BRAIN
ORIGINAL ARTICLE

Store-operated calcium entry is reduced in spastin-linked hereditary spastic paraplegia

Tania Rizo,[1] Lisa Gebhardt,[2] Julia Riedlberger,[1] Esther Eberhardt,[3,†] Lars Fester,[4] Dalia Alansary,[5] Jürgen Winkler,[6,7] Soeren Turan,[8] Philipp Arnold,[9] Barbara A. Niemeyer,[5,‡] Michael J. M. Fischer[2,10,‡] and Beate Winner[1,7]

‡These authors contributed equally to this work.

Pathogenic variants in *SPAST*, the gene coding for spastin, are the single most common cause of hereditary spastic paraplegia, a progressive motor neuron disease. Spastin regulates key cellular functions, including microtubule-severing and endoplasmic reticulum-morphogenesis. However, it remains unclear how alterations in these cellular functions due to *SPAST* pathogenic variants result in motor neuron dysfunction. Since spastin influences both microtubule network and endoplasmic reticulum structure, we hypothesized that spastin is necessary for the regulation of Ca^{2+} homeostasis via store-operated calcium entry.

Here, we show that the lack of spastin enlarges the endoplasmic reticulum and reduces store-operated calcium entry. In addition, elevated levels of different spastin variants induced clustering of STIM1 within the endoplasmic reticulum, altered the transport of STIM1 to the plasma membrane and reduced store-operated calcium entry, which could be rescued by exogenous expression of STIM1. Importantly, store-operated calcium entry was strongly reduced in induced pluripotent stem cell-derived neurons from hereditary spastic paraplegia patients with pathogenic variants in *SPAST* resulting in spastin haploinsufficiency. These neurons developed axonal swellings in response to lack of spastin. We were able to rescue both store-operated calcium entry and axonal swellings in *SPAST* patient neurons by restoring spastin levels, using CRISPR/Cas9 to correct the pathogenic variants in *SPAST*.

These findings demonstrate that proper amounts of spastin are a key regulatory component for store-operated calcium entry mediated Ca^{2+} homeostasis and suggest store-operated calcium entry as a disease relevant mechanism of spastin-linked motor neuron disease.

1 Department of Stem Cell Biology, Friedrich-Alexander-Universität Erlangen-Nürnberg, 91054 Erlangen, Germany
2 Institute of Physiology and Pathophysiology, Friedrich-Alexander-Universität Erlangen-Nürnberg, 91054 Erlangen, Germany
3 Department of Anesthesiology, Friedrich-Alexander-Universität Erlangen-Nürnberg, 91054 Erlangen, Germany
4 Institute of Anatomy and Cell Biology, Friedrich-Alexander-Universität Erlangen-Nürnberg, 91054 Erlangen, Germany
5 Molecular Biophysics, University of Saarland, Center for Integrative Physiology and Molecular Medicine, 66421 Homburg/Saar, Germany
6 Department of Molecular Neurology, Friedrich-Alexander-Universität Erlangen-Nürnberg, 91054 Erlangen, Germany
7 Center of Rare Diseases Erlangen (ZSEER), Friedrich-Alexander-Universität Erlangen-Nürnberg, 91054 Erlangen, Germany

Received January 12, 2021. Revised March 17, 2022. Accepted March 22, 2022. Advance access publication July 28, 2022

8 Institute of Biochemistry (Emil-Fischer-Center), Friedrich-Alexander-Universität Erlangen-Nürnberg, 91054 Erlangen, Germany
9 Institute of Anatomy, Functional and Clinical Anatomy, Friedrich-Alexander-University Erlangen-Nürnberg, 91054 Erlangen, Germany
10 Center of Physiology and Pharmacology, Medical University of Vienna, 1090 Vienna, Austria

† **Present address: Department of Anesthesiology, RWTH Aachen University, 52074 Aachen, Germany**

Correspondence to: Beate Winner
Department of Stem Cell Biology
Friedrich-Alexander University Erlangen-Nürnberg
Glückstraße 6
91054 Erlangen, Germany
E-mail: beate.winner@fau.de

Keywords: spastin; STIM1; microtubules; endoplasmic reticulum; store-operated calcium entry

Abbreviations: CRISPR = clustered regularly interspaced short palindromic repeats; dSTORM = direct stochastic optical reconstruction microscopy; ER = endoplasmic reticulum; GC = genome corrected; HSP = hereditary spastic paraplegia; iPSC = induced pluripotent stem cell; NPC = neural precursor cell; PM = plasma membrane; SOCE = store-operated calcium entry; TIRF = total internal reflection fluorescence

Introduction

Pathogenic variants in the *SPAST* gene result in spastin haploinsufficiency and are responsible for up to 40% all autosomal dominant cases of hereditary spastic paraplegia (HSP).[1–3] HSP is a group of monogenic motor neuron disorders, which result in progressive spastic paraplegia.[4,5] Spastin is not only a powerful microtubule-severing protein,[6–8] but also plays a role in remodelling the endoplasmic reticulum (ER) in axons.[9] Two main isoforms exist: a 68 kDa full length M1-spastin, and a 60 kDa ubiquitously expressed M87-spastin lacking the first 86 amino acids.[6,10] Although present in most tissues, M1-spastin is most strongly expressed in nervous tissues [6,11] and localizes to membranous cellular organelles, including the ER, via its N-terminal hydrophobic hairpin domain.[12,13] The M87-spastin isoform lacks this N-terminal domain.

The ER is the major intracellular Ca^{2+} store.[14,15] Decreases in ER luminal Ca^{2+} are detected by the ER resident protein stromal interaction molecule 1 (STIM1), which, upon unbinding of Ca^{2+} changes its conformation and oligomerizes.[16] STIM1 then tracks microtubules plus ends[16,17] and relocates within the ER membrane towards sites where the ER membrane is in close proximity to the plasma membrane (PM) to activate store-operated calcium entry (SOCE).[17–19] On these ER-PM junctions, STIM1 activates Ca^{2+} channels allowing the rapid influx of extracellular Ca^{2+} into the cytosol, triggering a broad range of key cellular mechanisms, including refilling of ER Ca^{2+},[20] activation of gene expression[21] and maintenance of dendritic spines.[22] Both decreased or increased levels of ER Ca^{2+} content have been implicated as drivers of neurodegenerative disorders with decreased ER Ca^{2+} leading to synaptic loss in Alzheimer's disease and decreased pace making in Parkinson's disease.[23,24] Increased ER Ca^{2+} resulted in altered mitochondrial ability to store Ca^{2+} in Huntington's disease[25] and release of neurotoxic factors from astrocytes in amyotrophic lateral sclerosis.[23,26]

Although SOCE has been investigated in many different types of cells, the mechanism by which it is regulated in human neurons, remains elusive. It is not entirely clear which ER and microtubule network-linked proteins are associated with this process. Studies investigating the role of the cytoskeleton in SOCE showed a decrease in SOCE as a consequence of microtubule network disruption after applying microtubule destabilizing agents such as nocodazole.[15] Interestingly, microtubule destabilization has been reported to have a direct impact on the ER-protein lateral mobility[27] and on the ER structure,[28] which in turn alters SOCE.[29] Collectively, this evidence suggests a direct link between the microtubule-regulated ER structure and Ca^{2+} signalling.

Since spastin influences both the microtubule network and the ER structure,[30] we hypothesized that spastin has an impact on the regulation of Ca^{2+} via SOCE in human neurons. We previously demonstrated that neurons derived from these SPAST-HSP patient induced pluripotent stem cells (iPSCs), besides expressing less spastin, display an altered microtubule network and develop a high degree of neurite swellings.[11,31–33]

Here, we demonstrate that lack of spastin decreases the Ca^{2+} re-uptake after ER-store depletion. We further describe how different parts of the spastin protein might alter the dynamics and distribution of STIM1 along the ER and to the PM. To test the significance of this mechanism for human neurons, we generated cortical neurons from the iPSCs from healthy donors, from patients with pathogenic variants in *SPAST*, and from clustered regularly interspaced short palindromic repeats (CRISPR)/Cas9-corrected isogenic controls and tested their capacity to regulate SOCE. We show that re-uptake of Ca^{2+} via SOCE is reduced in SPAST-HSP cortical neurons when compared to neurons derived from isogenic controls. In summary, our data describe how pathogenic spastin variants compromise neuronal Ca^{2+} homeostasis via SOCE, potentially increasing the vulnerability of neurons in SPAST-HSP.

Material and methods

Patient information and human iPSC derivation

SPAST-HSP patients and healthy donors were examined and diagnosed at the Department of Molecular Neurology of the Universitätsklinikum Erlangen (Germany), which also obtained the informed consent. The two SPAST patients were white females with European ancestry, with confirmed heterozygous pathologic variants in c.1684C>T and had typical clinical characteristics of pure spastic paraplegia. Patient UKER552 (hereafter referred to as Patient A) and patient UKERS3L (hereafter referred to as Patient B) were biopsied at 48 and 51 years of age, respectively. The healthy

donor UKER33Q (hereafter referred to as Control) was a 46-year-old, unrelated, white female with European ancestry and no history of neurological disorder (Supplementary Table 1).

Culture of embryonic stem cell, iPSCs and genome corrected iPSCs

Fibroblasts from SPAST patients and control were obtained by the Department of Molecular Neurology from dermal punch biopsies of the upper arm, after Institutional Review Board approval (consent #4120). These fibroblasts were reprogrammed into iPSCs via retroviral transduction of the transcription factors Klf4, c-Myc, Oct4 and Sox2 as previously described.[11,33,34] In brief, fibroblasts cultured in IMDM supplemented with 15% foetal bovine serum (FBS) (both Invitrogen) were seeded onto six-well plates (Corning) and for retroviral transduction 'spinfected' three times (800 *g* for 60 min; 8 µg/µl Polybrene) within 48 h with supernatant containing Sox2-, Klf4-, c-Myc- and three times the amount of Oct4 retrovirus. Twenty-four hours after the last spinfection, the fibroblasts were detached using TrypLE Express (Invitrogen) and cultured on a feeder layer of mouse embryonic fibroblasts (EMD Millipore) in human embryonic stem cell (hESC) medium containing Dulbecco's modified Eagle medium (DMEM)/F12/GlutaMAX, 20% Knockout Serum Replacement, 1× NEAA (all Invitrogen), 55 µM β-mercaptoethanol (Sigma-Aldrich), 20 ng/ml fibroblast growth factor 2 (FGF2; PeproTech) and 10 µM SB431542 (Sigma-Aldrich). Appearing colonies after ∼12 days were manually picked and transferred onto 24-well plates coated with 0.5 mg Matrigel (Corning) and further on cultured with mTeSR1 medium (STEMCELL Technologies). HUES6 (RRID: CVCL_B194, registered according to the German stem cell act approval #63 to Beate Winner), iPSCs and genome corrected iPSCs were clonally expanded using collagenase IV (Invitrogen) or Gentle Cell Dissociation Reagent (STEMCELL Technologies). The identity of iPSC and isogenic iPSC lines was corroborated by paternity testing. Karyotype was confirmed by G-Banding and genomic stability confirmed by copy number variation (CNV) analysis (all performed by the Department of Human Genetics in Erlangen). Pluripotency was characterized via flow cytometry of Tra-1-60 (BioLegend) and by immunofluorescence staining of of Oct4 (Santa Cruz) and Nanog (R&D Systems), and TRA1-60 (Millipore) and Nanog (R&D Systems). The ability to generate all of the embryonic germ layers after undirected *in vitro* differentiation was previously demonstrated.[11]

Generation of stem cell-derived neuronal cultures

Neural precursor cells (NPCs) and neurons were differentiated and characterized as previously described[11,33] (Supplementary Fig. 3). Briefly, ESCs and iPSCs were transferred to ultra-low attachment plates (Corning) to generate embryoid bodies (EBs) and cultured for 24 h on mTeSR1 (STEMCELL Technologies). The media was replaced with DMEM/F12 + GlutaMAX supplemented with N2 and B27 (without Vitamin A) and cultured for 1 week with fresh media change every other day (all Invitrogen). Embryoid bodies were then plated on poly-L-Ornithine (PLO, 10 µg/ml) and laminin- (5 µg/ml) (Invitrogen) coated plates and cultured one further week. Forming rosettes were manually picked under a stereomicroscope (Olympus). The neural rosettes were dissociated using TrypLE Express (Invitrogen) to form proliferative NPC lines. NPCs were grown on PLO/laminin-coated plates in DMEM/F12 + GlutaMAX supplemented with N2 and B27 (without Vitamin A) media supplemented with 20 ng/ml FGF2 (R&D Systems). Every 5–10 days the NPCs were split using TrypLE Express (Invitrogen) using a ∼1:3 ratio. Neuronal differentiation was initiated by seeding NPCs at low confluency (∼50 000 cells/cm^2) in N2 and B27 (without Vitamin A). Twenty-four hours after, the media was replaced by differentiation media [DMEM/F12 + GlutaMAX supplemented N2 and B27 (without Vitamin A), 20 ng/ml brain-derived neurotrophic factor (BDNF), 20 ng/ml glial cell line–derived neurotrophic factor (GDNF) (both Peprotech), 1 mM dibutyryl-cyclic adenosine monophosphate (cAMP) (AppliChem) and 200 nM ascorbic acid (AA)] (Sigma-Aldrich). Neurons were cultured for 4–5 weeks, changing three-quarters of the media every 3–4 days.

For patch clamp analysis, NPCs were seeded onto mouse astrocytes from CD1 mice (ScienCell, cultured according to the vendor's recommendation) and differentiated for 5 weeks. For patch clamp, the differentiation media was supplemented with 0.5% FBS (Invitrogen). The NPCs derived from ESCs, iPSCs and isogenic lines were sequenced for the presence or absence of the *SPAST* mutation (LGC Genomics) using sequencing primers fwd 5′-GTCAGTTGGCCACCAGTAGT -3 and rev 5′-ACTTCTTAAA CTTCTAAGGTGGT -3. All cultures were regularly tested for mycoplasma (Mycoalert, Lonza).

Cell culture of HEK293T cells and *SPAST* KO generation

HEK293T cells were cultured in IMDM supplemented with 10% FBS and 1× Penicillin/Streptomycin (all Invitrogen) in T75 Flasks (Sarstedt). Confluent cells were passaged every 3–4 days using TrypLE Express (Invitrogen) and seeded one day before transfection. PEI/DNA (4:1 ratio) complexes were formed in OPTI-MEM (Invitrogen) and added to cells on antibiotic free media. After 4 h, the media was changed to full media containing FBS and antibiotics. The cells were analysed or fixed 24 h post-transfection. To generate *SPAST* KO cells, sgRNAs were designed using the CRISPOR online tool (http://crispor.tefor.net/).[35] The Oligonucleotides containing sgRNAs (spacer sequence is depicted in bold) (5′-CACCG**gaatagctgttatagttac**-3′; 5′-AAAC**gtaactataacagctattc**C-3′ both Sigma-Aldrich) were cloned into the vector backbone pCAG-SpCas9-GFP-U6-gRNA (Addgene #79144) using an adapted version of the protocol developed by the Zhang Lab (https://www.addgene.org/crispr/zhang/). Briefly, the vector backbone was digested using BbsI-HF (NEB), CutSmart Buffer (NEB) and dephosphorylated with Calf Intestinal Alkaline Phosphatase (CIP, NEB). The sgRNAs were annealed and phosphorylated with the T4 Polynucleotide Kinase (NEB) using the following thermocycler protocol: 30 min at 37°C, 5 min at 95°C, ramp down to 25°C at 5°C/min. Annealed sgRNAs and digested backbone were ligated using the Quick Ligase (NEB). Ligation reaction was electroporated and propagated in GeneHogs E.Coli (Invitrogen). Endotoxin-free purified plasmids (Machery-Nagel) were transfected into HEK293T cells using polyethylenimine (PEI). After 48 h single cells were FACS sorted into 96-well plates. Genomic DNA from growing colonies was extracted using DNA Quickextract (Epicentre) and PCR amplified using primers for the expected cutting side (5′-CTCACGGCCCCAAAATGTTG-3′, 5′-CTGAAATCTGGACAATCAT GTGAA-3′ both Sigma-Aldrich). After PCR gel purification, PCR products were sequenced (LGC Genomics) using the same primers for PCR amplification. Sequencing reads were analysed for InDels using A Plasmid Editor (*aPE*; University of Utah; Salt Lake City, UT) and Tracked Indel DEcomposition (TIDE) genotyping analysis.[36] For further confirmation of insertion–deletion mutations (InDels), PCR products of spastin KO and wild-type cell lines were sent for

next generation-based amplicon sequencing (GENEWIZ) using the same PCR amplification primers (Supplementary Fig. 1E).

Genome editing of iPSCs

Genome correction of the SPAST mutation in iPSCs was carried out by Applied StemCell. For this purpose, one iPSC clone from SPAST Patient A (UKERi552-R1-008) and one iPSC clone from SPAST Patient B (UKERiS3L-R1-014) were sent to Applied StemCell for the generation of SPAST isogenic lines. Applied StemCell used the CRISPR/Cas9 system to correct the non-sense mutation in SPAST patients c.1684C>T/p.R562X, het. in exon 15 of the gene *SPAST*. The purchased genome corrected clones were hereafter referred to as SPAST GC A (UKERi552-R1-SC1-008 which is an isogenic line from Clone UKERi552-R1-008) and SPAST GC B (UKERiS3L-R1-SC1-014 and UKERiS3L-R1-SC2-014 which are isogenic lines from UKERiS3L-R1-014). Genotype of iPSCs was confirmed by the Center of Human Genetics, Regensburg University (Prof. Ute Hehr).

DNA constructs

M1-spastin-IRES-GFP, M87-spastin-IRES-GFP and myc-DM87-spastin-IRES-GFP were used for all Ca^{2+} imaging measurements. From these constructs, only the vector expressing DM87 was myc tagged to aid detection via western blot or immunofluorescence. Since the spastin proteins were not fluorescently tagged, IRES-GFP was used as a reporter to detect transfected cells. These constructs were generated by subcloning the M1 or M87-spastin sequence of pLXIN-myc-spastin. pLXIN-myc-spastin expression vector was previously generated and kindly provided by Evan Reid.[37] To PCR amplify M1-spastin following primers with NheI and BsiWI overhangs were used 5′-GCTAGCACCATGAATTCT CCGG-3′ and 5′-CGTACGCGTTTAAACAGTGGTATCTCCA-3′. M87-spastin PCR amplified using the primers with NheI and BsiWI overhangs 5′-GCTAGCACCATGGCAGCCAAGAGGAGCT-3′ and 5′-CGTACGCGTTTAAACAGTGGTATCTCCA-3′. Myc-DM87 was PCR amplified using following primers with NheI and BsiWI overhangs 5′-GCTAGCACCATGAATTCTCCGG-3′ and 5′-CGTACGCGTGAGGGC GCGGGAGAAGCGC-3′. M1-spastin, M87-spastin and DM87-spastin were then inserted (NheI-BsiWI) into a pCSC-SP-PW-GFP (aka: pBOB-GFP), which was a kind gift from Inder Verma (Addgene plasmid # 12337; http://n2t.net/addgene:12337; RRID:Addgene_12337). The expression vectors mCherry-STIM1 to express STIM1 and pEF1-dTomato to visualize single neurons were previously reported.[11,38] For immunofluorescence the following myc-tagged vectors were generated and employed: pCMV6-Entry-*SPAST*(M1)-myc tagged vector was obtained from Origene. pCMV6-Entry-*SPAST*(M87)-myc tagged vector was generated by PCR amplifying the M87-spastin sequence from the pCMV6-Entry-*SPAST*(M1)-myc using following primers with NheI and Acc3 overhangs 5′-TAGCTAGCATGGCAGCCAAGAGGAGCTC-3′ and 5′-TATTTCCGG ATGCAGCTCTCGG-3′. Sequences were inserted (Nhe1-Acc3) into the digested target vector pCMV6-Entry-*SPAST*(M1)-myc. The myc tag aided the detection for immunofluorescence. Cas9-plasmid pCAG-SpCas9-GFP-U6-gRNA was a gift from Jizhong Zou (Addgene plasmid # 79144; http://n2t.net/addgene:79144; RRID: Addgene_79144).

Intracellular Ca^{2+} imaging

Neurons were differentiated for four weeks before Ca^{2+} imaging measurements (Supplementary Tables 1–3 for information about the lines). HEK293T cells were measured the day after transfection. To detect ratiometric Ca^{2+} changes, cells were loaded with 3 µM Fura-2 AM and 0.02% Pluronic F-127 (both Biotium) for 30 min at 37°C and 5% CO2. In the case of neurons, Fura-2 AM and Pluronic F-127 was diluted into corresponding growing media. In the case of HEK293T cells, Fura-2 AM and Pluronic F-127 was diluted into standard external solution (145 mM NaCl, 5 mM KCl, 1.25 mM $CaCl_2$,1 mM $MgCl_2$, 10 mM Glucose, 10 mM HEPES, ∼308–312 Osm). For the Ca^{2+}-free external solution, $CaCl_2$ was replaced by 10 mM EGTA. The experiment was performed in continuous gravity-driven laminar superfusion from a common outlet. The experimental protocol was preprogrammed, the pinch-valves were controlled by a WAS02 synchronized to the acquisition.[39] The protocol consisted of incubating the cells in Ca^{2+}-free external solution for 10 min after Fura-2 staining and before the recording. A 2 min baseline was recorded in calcium-free external solution, then 2 µM Thapsigargin (Calbiochem) in Ca^{2+}-free solution was applied for 5 min, followed by a 1 min wash out with Ca^{2+}-free external solution. The cells were then exposed for 5 min to Ca^{2+}-containing external solution to detect Ca^{2+} entry. Ca^{2+}-free external solution was superfused for five further minutes.

To measure the intracellular calcium levels, Fura2 was excited using a Polychrome V monochromator (Till Photonics) to produce light pulses at alternating wavelengths of 358 nm and 391 nm at a frequency of 1 Hz. The respective Fura-2 fluorescence emission >440 nm was recorded using a Peltier-cooled slow-scan CCD camera and the TILLvisION software package (Till Photonics). For cells transfected with the GFP constructs, an additional image at 488 nm was acquired to select for GFP positive cells. GFP fluorescence excitation at 358 nm and 391 nm in relation to excitation at 488 nm was quantified and was subtracted from the 358 and 391 nm excitation. Regions of interest were manually selected avoiding high GFP or mCherry expressing cells. In neurons, regions of interest were placed inside neuron somas. Fluorescence ratio (F358/391) is reported as mean with 95% confidence intervals.

Analysis of mCherry-STIM1 translocation

Wild-type HEK293T cells were plated onto #1.5H dishes with glass coverslip (Ibidi). The following day, the cells were transiently transfected with mCherry-STIM1 and either CAG-IRES-GFP (empty vector), CAG-M1-spastin-IRES-GFP, CAG-M87-spastin-IRES-GFP or CAG-DM87-spatin-myc-IRES-GFP. The following day, for total internal reflection fluorescence (TIRF) imaging, the culture media was replaced by TIRF extracellular solution before recording (145 mM NaCl, 1 mM $CaCl_2$, 2 mM $MgCl_2$, 4 mM KCl, 10 mM glucose and 10 mM HEPES, pH 7.4). For the mCherry-STIM1 translocation assay, TIRF Ca^{2+} -free solution (145 mM NaCl, 1 mM EGTA, 2 mM $MgCl_2$, 4 mM KCl, 10 mM glucose and 10 mM HEPES, pH 7.4) was supplemented with 2 µM thapsigargin and was added 1:1 to reach a concentration of 1 µM Thapsigargin immediately before recording. Images were acquired every 5 s for 10 min. TIRF recordings were conducted on a Leica DMi8 TIRF system equipped with a 100× 1.47 NA oil HC PL Apo objective and a CMOS camera (Hamamatsu) or a EMCCD camera iXon 885 (Andor). The penetration depth of the evanescent field was set to 150 nm. Quantification of the STIM1 cluster was done using ImageJ software (National Institutes of Health). For this purpose, the first image was subtracted from the time series. The background was subtracted using a rolling ball radius of 50 pixels. The image was thresholded on the last frame using the Otsu algorithm. To separate clusters, thesholded images were binarized and the built-in hole-filling and watershed algorithms were used. The particles were analysed using the particle analyser setting a minimum particle recognition size of

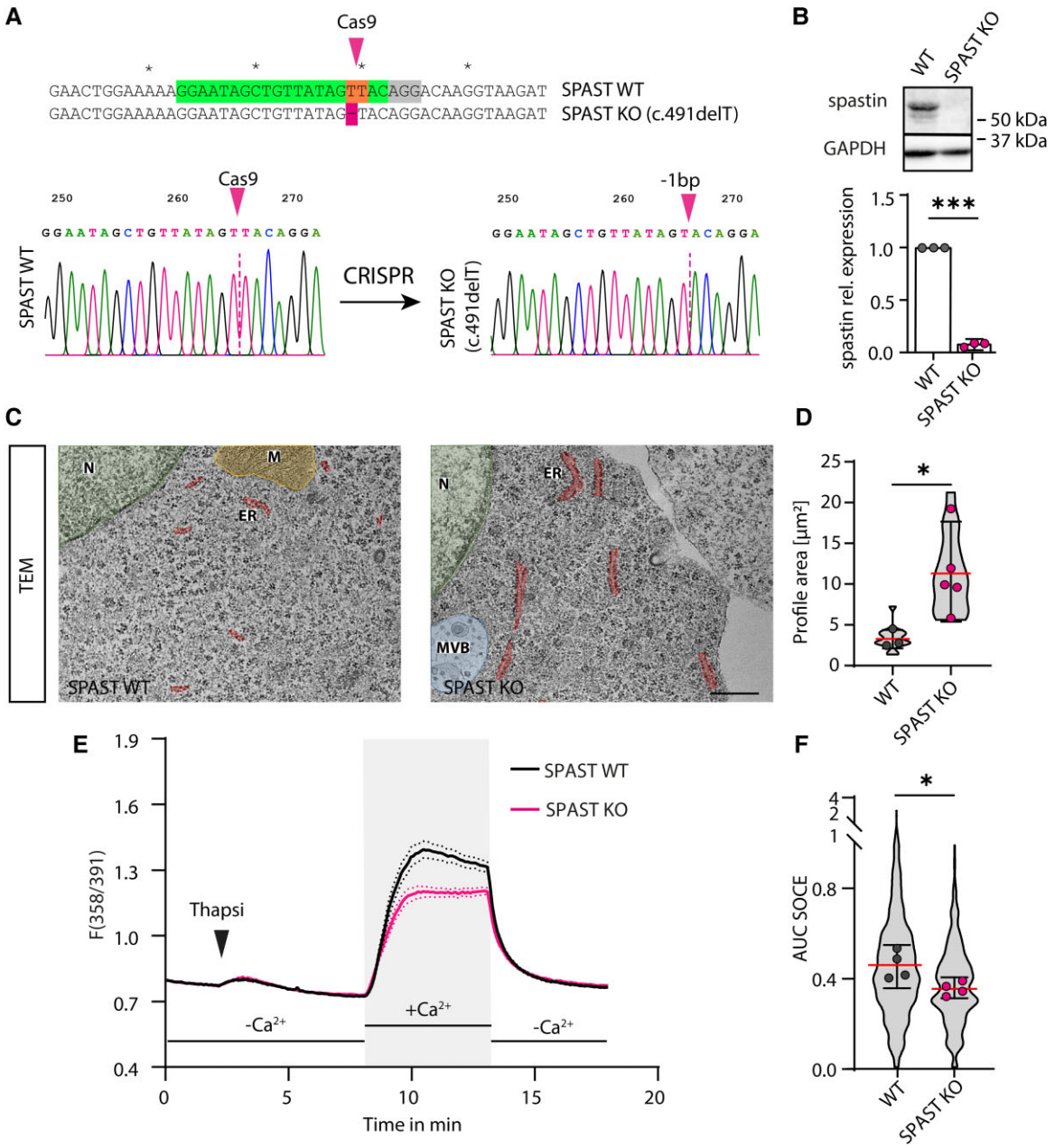

Figure 1 CRISPR/Cas9 generated SPAST KO in HEK293T cells impairs SOCE. (**A**) Genomic region (*top row*) in Exon 2 of SPAST (WT). A –1 bp deletion (c.491delT SPAST KO) was generated using CRISPR/Cas9 (*bottom row*). Single guide RNA (sgRNA, green), PAM region (grey), cutting site (orange) and bp deletion (magenta). The lower panel displays the sequencing of SPAST WT HEK293T cells before and after CRISPR/Cas9 induced –1bp deletion. (**B**) Western blot of wild-type (WT) and spastin knockout (SPAST KO) cells probed for spastin and GAPDH used as a housekeeping control. Spastin is depleted in SPAST KO cells [$t(4) = 83.43$; $P < 0.001$ unpaired two-tailed *t*-test]. Data shown as mean ± standard error of the mean (SEM). (**C**) Transmission electron microscopy (TEM) images of SPAST KO or WT HEK293 cells with the nucleus (N, green), mitochondria (M, orange), endoplasmic reticulum profiles (ER, red) and multi vesicular bodies (MVB, blue) shown in false colour. Scale bar = 500 nm. (**D**) Quantification of ER profile areas comparing wild-type and SPAST KO 293 T cells [unpaired two-tailed *t*-test, $t(6) = 2.70$, $P = 0.036$]. Each data point indicates the mean size of the ER profiles in one cell (WT $n = 3$; SPAST KO $n = 5$ cells). The scatter plot shows the mean of cells±95% confidence interval. The violin plot shows the distribution of the measured ER profiles (15 ER profiles per group). (**E**) Fura-2 fluorescence ratio changes *F*(358/391) were analysed in WT HEK293T cells and compared to SPAST KO HEK293T cells. Ca^{2+} imaging recording started in absence of Ca^{2+}. For additional depletion of ER Ca^{2+} stores 2 µM Thapsigargin (Thapsi) was added. Perfusion with Ca^{2+} rich media triggered SOCE, quantified as area under the curve [AUC, grey box. Data shown as mean SOCE response (line)±95% confidence interval (dotted line)]. (**F**) Depletion of spastin significantly decreases SOCE [Unpaired two-tailed *t*-test. $t(6) = 3.065$. $P = 0.022$]. Each data-point represents the median SOCE response of the cells of one experimental day ($n = 4$ experimental days per group). The scatter plot shows the mean of experimental days±95% confidence interval. The violin plot shows the distribution of single cells (SPAST KO cells = 970; SPAST WT cells = 1065). *$P < 0.05$ **$P < 0.01$ ***$P < 0.001$, n.s. = not significant.

0.03 µm^2 particle size. The number of particles normalized to the cell footprint area was plotted over time. Pre-clustered cells (cells with five or more clusters at the beginning) were excluded. To assess the kinetics of STIM1 and determine the Boltzmann-slope (dX) single traces were fit into a Boltzmann-Sigmoid nonlinear curve using GraphPad Prism 8 Software (GraphPad Software, Inc.). The relative and cumulative frequency distribution of the particle size was also calculated using GraphPad Prism 8 Software.

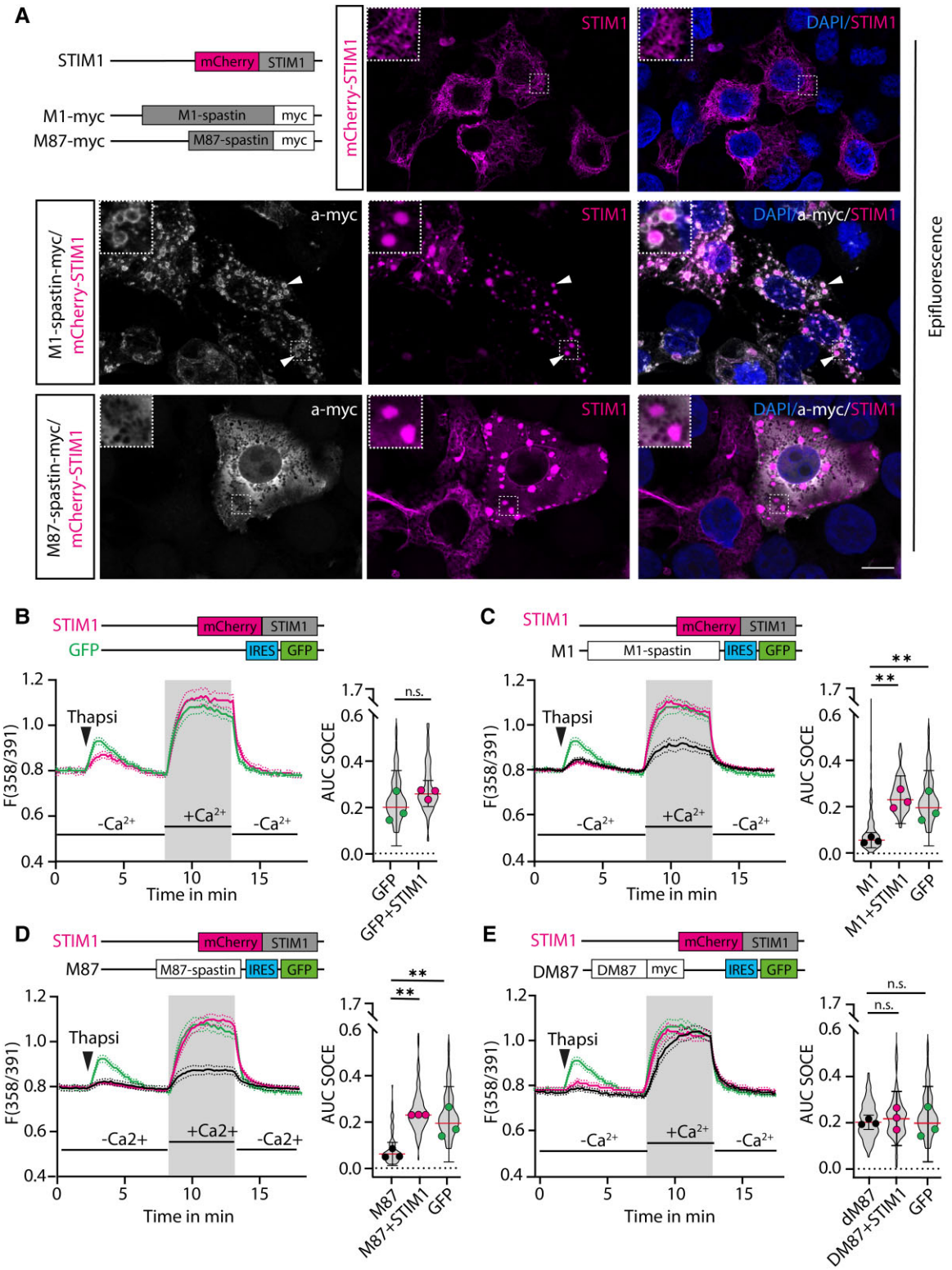

Figure 2 Spastin overexpression alters the distribution of STIM1 and reduces SOCE. (**A**) In HEK293T cells, mCherry-STIM1 shows a reticular distribution when expressed alone. In the presence of M1- or M87-spastin-myc, mCherry-STIM1 clusters. Only M1-spastin-myc encloses mCherry-STIM1 clusters (white arrowheads). The mCherry-STIM1 (STIM1), M1-spastin-myc, M87-spastin-myc expression vectors used to assess the intracellular distribution of STIM1 are displayed in the *top left* corner. Scale bar = 10 µm. (**B–E**) Fura-2 fluorescence ratio changes F(358/391) analysed in HEK293T cells expressing (**B**) IRES-GFP (GFP, green line) alone or in combination with mCherry-STIM1 (STIM1, pink line), (**C**) M1-spastin-IRES-GFP (M1, black line) alone or in combination with STIM1 (pink line), (**D**) M87-spastin-IRES-GFP (M87, black line) alone or in combination with STIM1 (pink line) and (**E**) DM87-myc-spastin-IRES-GFP (DM87, black line) alone or in combination with STIM1 (pink line). (**C–E**) The GFP control is displayed in green. (**B–E**) The Ca^{2+} imaging recording started in absence of Ca2+. For maximal depletion of Ca^{2+} from the ER stores, the cells were superfused with 2 µM Thapsigargin (Thapsi) for 5 min. Perfusion with Ca^{2+} rich media triggered SOCE, quantified as area under the curve [AUC, grey box.

(Continued)

Patch clamp analysis

Mature neurons to be patched were selected by NeuroFluor NeuO (STEMCELL Technologies) staining (Supplementary Tables 1–3 for information about the lines). The live-dye was used according to manufacturer's instructions at 0.125 µM NeuO, diluted in neuronal differentiation media. Whole-cell patch clamp recordings were conducted at room temperature using a HEKA EPC-10USB amplifier (HEKA Elektronik) and recorded using the PatchMaster software (HEKA Elektronik). For current-clamp experiments, the holding potential was set to –70 mV.

Cell cultures were recorded under constant perfusion with artificial CSF (ACSF, in mM: 125 NaCl, 3 KCl, 1 $CaCl_2$, 1 $MgCl_2$, 1.25 NaH_2PO_4, 25 $NaHCO_3$ and 10 d-glucose; pH 7.4, ~ 295–305 Osm) bubbled with 95% O_2 and 5% CO_2. The internal solution contained (in mM) 4 NaCl, 135 K-gluconate, 3 $MgCl_2$, 5 EGTA, 5 HEPES, 2 Na_2-ATP and 0.3 Na_3-GTP (pH 7.25, Osm ~290). Borosilicate glass capillaries with a resistance between 3.0 and 6 MΩ were pulled using a DMZ Universal Pipette puller (Zeitz Instruments). The recordings were analysed using HEKA Fitmaster software and IGOR 5.0.

Immunocytochemistry

Cells were fixed for 20 min at room temperature in 4% paraformaldehyde (PFA) in phosphate-buffered saline (PBS) (w/v), washed three times with PBS and permeabilized for 10 min in PBS containing 0.1% Triton X-100 (v/v) (Sigma-Aldrich). In the case of mCherry-STIM1 transfected cells, permeabilization was carried out in 0.5% Saponin (w/v) in PBS. Non-specific antibody binding was blocked by incubating cells for 30 min on PBS supplemented with 5% donkey serum (v/v) (Pan Biotech). The coverslips were incubated with primary antibodies overnight at 4°C in a buffer containing PBS supplemented with 0.3% donkey serum and either 0.01% Triton X-100 or 0.05% Saponin. Myc, calreticulin and Lamp1 (all Abcam) were incubated in Saponin containing buffer. TUBB3 (Biolegend or Abcam), Nestin (Millipore), SOX2 (Cell Signaling), GFAP (DAKO), Oct3-/4 (Santa Cruz) and Nanog (R&D Systems) were incubated in Triton X-100 containing buffer. After three washes with PBS (5 min each), secondary HRP antibodies (Thermo Scientific) were incubated for 3 h at room temperature on PBS with 0.3% donkey serum and supplemented with either 0.01% TritonX-100 or 0.05% Saponin. The coverslips were washed twice with PBS, counterstained with 0.5 mg/ml 49,6-diamidino-2-phenylindole (DAPI) and mounted on microscope slides (Carl Roth) using a water-soluble mounting media (Aqua-poly/Mount, Polysciences). Unless otherwise stated, immunofluorescence images were acquired using a fluorescence microscope (Observer. Z1, Zeiss) equipped with an Apotome 2.0.

Electron microscopy

Transmission electron microscopy (TEM) was performed as described previously[40] with the exception that cells were grown on six-well plates (Corning) and after embedding plastic supports were removed by shock freezing in liquid nitrogen. After thin sectioning, samples were transferred to a JEM 1400 Plus TEM (JEOL) for imaging. TEM images were acquired at a nominal magnification of 15 000×. The obtained images were quantified using ImageJ. The ER profile area was measured wherever two opposing rows of ribosomes were present. The ribosomes on both sides were masked out and the area of the ER profile was quantified.

Direct stochastic optical reconstruction microscopy

For direct stochastic optical reconstruction microscopy (dSTORM) imaging, SPAST iPSC-derived neurons were seeded on 1.5H µDishes (Ibidi). To extract cytosolic proteins, the neurons were incubated at 37°C for 30 s with extraction buffer containing 0.25% v/v Triton X-100, 0.1% glutaraldehyde, 0.02% PFA in PIPES, EGTA and $MgCl_2$ buffer (PEM buffer 80 mM PIPES, 5 mM EGTA, 2 mM $MgCl_2$) and subsequently fixed with 0.25% Triton-X-100 and 0.5% glutaraldehyde at 37°C for 10 min. Fixation solution was replaced by 50 mM NH4Cl and incubated for 7 min. Non-specific targets were blocked in 1% bovine serum albumin (BSA) in PBS for 30 min. TUBB3 antibody was diluted in 1% BSA in PBS and incubated overnight at 4°C. After three 5-min washes with PBS, the neurons were incubated with AF647 antibody (Life Technologies) diluted in 1% BSA in PBS for 2 h at 37°C. To visualize nuclei, the neurons were incubated for 2 min in DAPI diluted in PBS. Neurons were post-fixed in 10% Formalin (Sigma) for 10 min, washed three times, 5 min each with PBS and stored in PBS. dSTORM imaging of stained neurons was performed with a SAFe180 3D super-resolution module (Abbelight) mounted on an Olympus Ix83 equipped with a 100×, NA 1.5 objective. For imaging, stained neurons were incubated in dSTORM buffer (Abbelight Smart Kit). Image acquisition, astigmatic 3D-localization, processing and reconstruction was performed using Abbelight Neo Software. Neo Software was also used for 3D visualization and analysis of localization data, together with ImageJ platform (ThunderStorm).

Western blot

Cell pellets were lysed with lysis buffer [1% NP-40, 150 mM NaCl, 25 mM Tris-HCL, 5 mM EDTA, EDTA free complete mini protease inhibitor cocktail (Roche), PhosSTOP (Roche), 1 mM PMSF] on ice and sonicated. Protein concentration was assessed by Bicinchoninic Acid (BCA) (Thermo Scientific). Protein samples were prepared with 2× Laemmli Buffer (62.5 mM Tris-HCl, pH 6.8, 25% glycerol, 2% SDS, 0.01% bromophenol blue and 0.5% β-mercaptoethanol) and boiled for 7 min at 95°C. Equal amounts of protein were used to run SDS-PAGE in Mini-Protean Tetra Cell gel systems (Bio-Rad). Separated proteins were blotted onto methanol pre-activated PVDF Membranes using Mini Trans-Blot Electrophoretic transfer cell system (Biorad). The membranes were blocked in 5% blotting-grade blocker (Biorad) diluted in Tris-buffered saline supplemented with Tween [TBS-T; TBS supplemented with 0.08% (v/v) Tween]. The membranes were incubated with primary antibodies overnight at 4°C. Antibodies STIM2 (Sigma) and Spastin (Abcam) were diluted in 1% blotting grade blocker in TBS-T. STIM1 (Cell Signaling), GAPDH

Figure 2 Continued
Data shown as mean (line) ± 95% confidence interval (dotted line)]. The quantification of the AUC SOCE is shown on the right side of the respective Fura-2 fluorescence ratio changes. [(**B**) Unpaired two-tailed *t*-test, $t(4) = 1.58$, $P = 0.19$; (**C**) one-way ANOVA, $F(2,6) = 12.99$, $P = 0.007$; Holm-Sidak's *post hoc*: M1 versus M1+ STIM1 $P = 0.006$, M1 versus GFP $P = 0.009$.(**D**) one-way ANOVA, $F(2,6) = 15.27$, $P = 0.004$. Holm-Sidak's *post hoc*; M87 versus M87+ STIM1 $P = 0.004$, M87 versus GFP, $P = 0.006$. (**E**) one-way ANOVA, $F(2,6) = 0.12$, $P = 0.89$]. Each data-point represents the median SOCE response of cells of one experimental day ($n = 3$ experimental days). The scatter plot shows the mean (red line) of the experimental days±95% confidence interval, the violin plot shows the distribution of single cells (Number of cells: GFP = 266; GFP+STIM1 = 248; M1 = 330; M1+STIM1 = 302; M87 = 215; M87+STIM1 = 250; DM87 = 282; DM87+STIM1 = 242). *P < 0.05 **P < 0.01 ***P < 0.001, n.s. = not significant.

(Millipore) and GRP78 (BD-Biosciences) were diluted in TBS-T. After 3× 15 min wash with 0.08% (v/v) TBS-T, the membranes were incubated for 1 h at room temperature with the secondary antibodies (Thermo Scientific). The blots were developed by using ECL blotting solution (Amersham), and chemiluminescence detected on X-ray films (Amersham) or automated detection system (ChemiDoc MP, Biorad) and quantified using ImageLab 6.0 (Biorad).

Statistical analysis

Statistical analysis was conducted using GraphPad Prism 8 Software (GraphPad Software, Inc.). Normal distribution was examined using the Shapiro-Wilk test. When comparing Gaussian distributed data either two-sided-unpaired *t*-test or a one-way ANOVA was conducted to compare more than two groups with a normal distribution. When comparing not Gaussian distributed data sets, either a Mann–Whitney U-test (two groups) was used or a Kruskal–Wallis ANOVA (for more than two groups) was used. *P*-values ≤ 0.05 were considered significant ($^{*}P \leq 0.05$, $^{**}P \leq 0.01$, $^{***}P \leq 0.001$).

Data availability

Additional data, material, and protocols are provided upon reasonable request to the corresponding author.

Results

CRISPR/Cas9 *SPAST* knockout in HEK293T cells impairs SOCE

To investigate the influence of reduced spastin levels on SOCE, we first generated spastin knockout (KO) HEK293T cell lines using CRISPR/Cas9 technology to generate a one base pair (bp) deletion in both *SPAST* alleles at c.491delT (Fig. 1A) in exon 2. The *SPAST* 1 base pair deletion was corroborated at the genome level via Sanger sequencing (LGC Genomics) and using next-generation sequencing (NGS)-based amplicon sequencing (Fig. 1A and Supplementary Fig. 1A and B). This deletion resulted in a frameshift (p.Val164fs) generating a predicted premature stop codon and the complete loss of spastin protein as confirmed by western blot (Fig. 1B).

To assess the impact of lack of spastin on the ER structure, we compared the ER structure of SPAST KO to wild-type HEK293T cells using TEM. The ER profile area was defined by presence of two opposing rows of ribosomes and quantified. SPAST KO cells displayed a larger average area per ER profile compared to wild-type cells (Fig. 1C and 1D).

Such ER enlargements are reported to interfere with the formation of STIM1-ORAI1 complexes and SOCE efficiency.[41] To test whether lack of spastin and associated altered ER structure had a similar impact on the ER calcium regulation via SOCE we conducted Fura-2-based Ca^{2+} imaging. We started the recording in Ca^{2+} -free conditions and additionally applied the Serca2-inhibitor Thapsigargin to maximally deplete the ER from Ca^{2+}. The fluorescence ratio [F(358/F391)] changes after Thapsigargin store depletion and after reperfusion with Ca^{2+}, corresponding to SOCE and were measured (Fig. 1E) and SOCE was quantified as area under the curve (AUC, Fig. 1F). The SOCE response was reduced in the SPAST KO compared to the SPAST wild-type cells (Fig.1E and F). In summary, these data indicate that the presence of spastin is important for maintaining the ER structure and the dynamic reshaping of the ER during store depletion and SOCE induction.

M1 and M87-spastin alter the distribution of STIM1 and reduce SOCE

Spastin, in addition to its ubiquitously expressed M87 isoform, is also expressed as M1 spastin which is mainly found in neuronal cells. To investigate spastin's isoform-dependent effect on the localization of STIM1, we expressed mCherry-STIM1 alone or in combination with M1 or M87-spastin-myc in HEK293T cells (Fig. 2A). The typical mCherry-STIM1 reticular distribution (Fig. 2A, upper lane) was changed to intense STIM1 clusters surrounded by M1-spastin ring-like structures or larger STIM1-clusters not surrounded by rings in case of M87 (Fig. 2A, lower lanes). These clusters co-labelled with the intraluminal ER marker calreticulin and were not labelled by the lysosomal marker LAMP-1, confirming ER localization (Supplementary Fig. 2A and B).

To understand the impact of the different spastin isoforms on SOCE, we conducted Ca^{2+} imaging on HEK293T expressing M1- or M87-spastin-IRES GFP and an additional truncated DM87-spastin-IRES GFP construct (containing only spastin's N-terminal domain) and used IRES-GFP (GFP) as the control (Fig. 2B–E and Supplementary Fig. 2C–E). As expected, in cells overexpressing M1-, or M87-spastin, the microtubule network was disassembled (Supplementary Fig. 2G) and SOCE was significantly decreased compared to the GFP control (Fig. 2B–D). This was not the case in the microtubule preserving DM87 spastin (Fig. 2E and Supplementary Fig. 2G). The protein amounts of STIM1, which could have accounted for the reduced SOCE[42] and the levels of the ER stress marker GRP78 were unchanged by overexpression of either of the spastin constructs (Supplementary Fig. 2F). We then reasoned that if the spastin-induced reduction in SOCE was the result of decreased mobility of STIM1 towards the plasma membrane contact sites, additional STIM1 would be able to rescue SOCE. Indeed, as shown in Fig. 2B–E, co-expression of mCherry-STIM1 in HEK293T cells expressing either M1- or M87-spastin significantly rescued the previously reduced SOCE (Fig. 2C and D). No changes were seen when combining mCherry-STIM1 and DM87 (Fig. 2B and E). In conclusion, these results indicate that the addition of STIM1 is sufficient to rescue the SOCE impairments elicited by expression of M1 or M87-spastin.

Spastin overexpression impairs the transport of STIM1 to the plasma membrane

Since STIM1 distribution in the ER and SOCE were reduced by altered levels of spastin, we next tested whether spastin had an impact on the relocation of STIM1 clusters, from the ER to the PM, a step that precedes the formation of active SOCE channels. We used live TIRF microscopy to visualize the formation of STIM1 clusters within 150 nm near the plasma membrane during 10 min of Thapsigargin induced Ca^{2+} store depletion in the presence of different spastin isoforms (Fig. 3A). The number of STIM1 clusters per μm^2 forming over time were fitted into a Boltzmann-sigmoid curve (Fig. 3B) to calculate the Boltzmann-slope factor, which describes how fast clusters are formed on the TIRF plane. The Boltzmann-slope factor returns high values for a less steep curve and lower values for steeper rise. The formation of STIM1 clusters at ER-PM junctions was significantly slower in the presence of M1 or DM87 spastin isoforms (Fig. 3B and C). M87 spastin induced only a mild effect on the translocation of STIM1. Additionally, the size of STIM1 clusters was strongly reduced in the presence of DM87-spastin and slightly reduced in the presence of M1-spastin (Fig. 3D and E). Together, these data indicate that, long before the

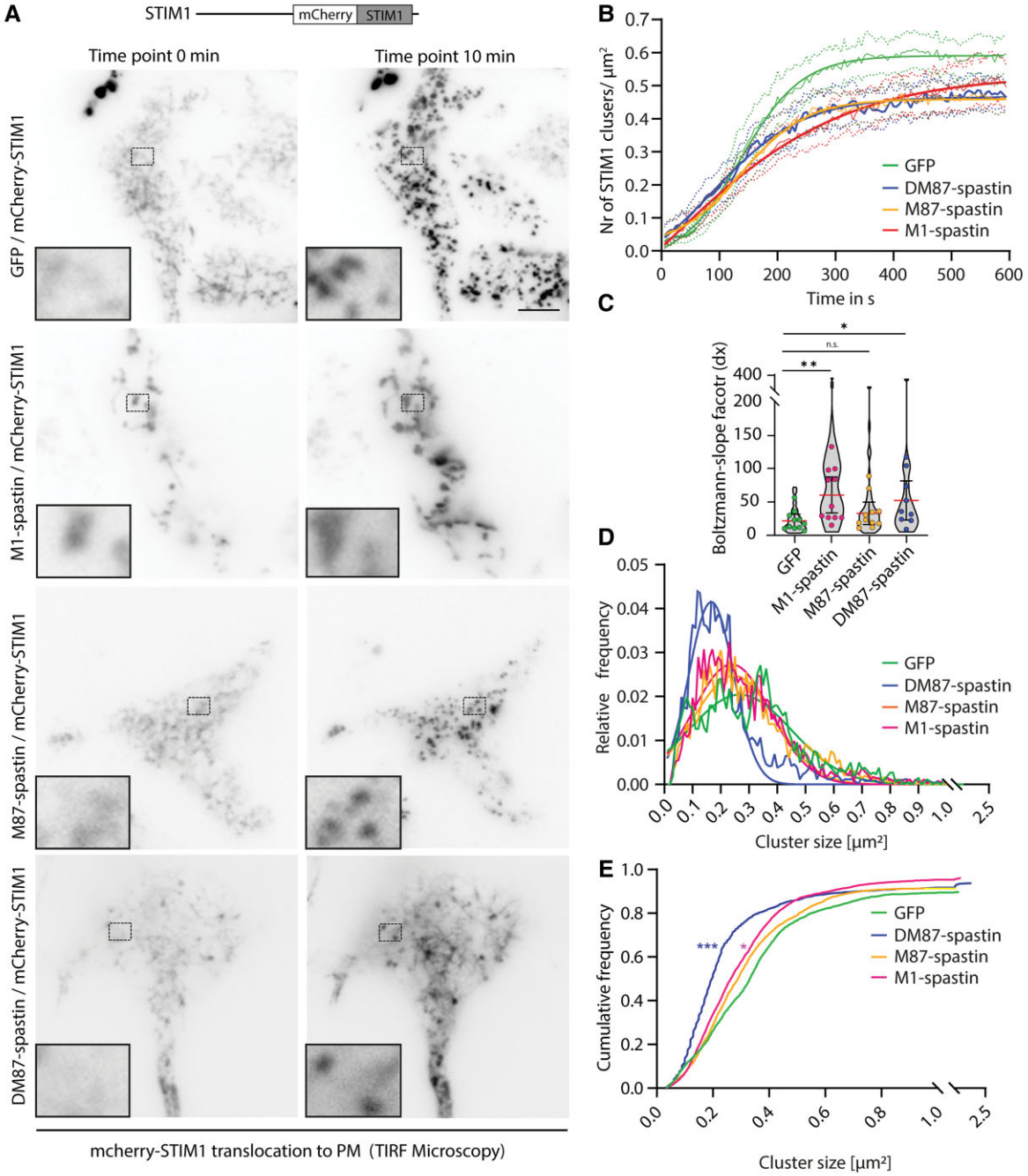

Figure 3 Spastin overexpression impairs the dynamic transport of STIM1 to plasma membrane. (**A**) HEK293T cells transfected with mCherry-STIM1 and either GFP, M1, M87 or DM87 spastin were imaged using TIRF microscopy. Representative TIRF images are shown before and after 10 min of store depletion induced by the addition of 1 µM Thapsigargin. Scale bar = 5 µm. (**B**) The number of mCherry-STIM1 forming clusters were normalized to the cell footprint area (µm^2) and plotted over time. The raw traces (continuous line) represent the mean ± 95% confidence interval (dotted line) of 5–6 experimental days, 9–11 recordings and a total of 31–46 cells. A Boltzmann-sigmoid curve was fitted to the mean raw data (bold continuous line). (**C**) The Boltzmann- slope factor was calculated (*dX*) and describes the steepness of the curve in (**B**), with higher values corresponding to less steep curves and slower appearance of STIM1 clusters. [Kruskal–Wallis-ANOVA, $H(3) = 9.58$, $P = 0.02$; uncorrected Dunn's, GFP versus M1 $P = 0.004$; GFP versus M87 $P = 0.26$, GFP versus DM87 $P = 0.02$]. Single data-points represent the median of one recording. The scatter plot shows the mean of recordings (red line) ± 95% confidence interval. The violin plot shows the distribution of the Boltzmann-slopes of single cells. (**D**) Relative frequency distribution of mCherry-STIM1 cluster size in HEK293T cells expressing GFP, M1, M87 or DM87-spastin and (**E**) calculated relative cumulative distribution of STIM1 clusters size. [Kolmogorov–Smirnoff test, Kolmogorov–Smirnov Distance (K-S D) GFP versus DM87 $P < 0.001$, K-S D = 0.37; GFP versus M1 $P = 0.01$, K-S D = 0.21; GFP versus M87 $P = 0.096$, K-S D = 0.16]. $^*P < 0.05$ $^{**}P < 0.01$ $^{***}P < 0.001$, n.s. = not significant.

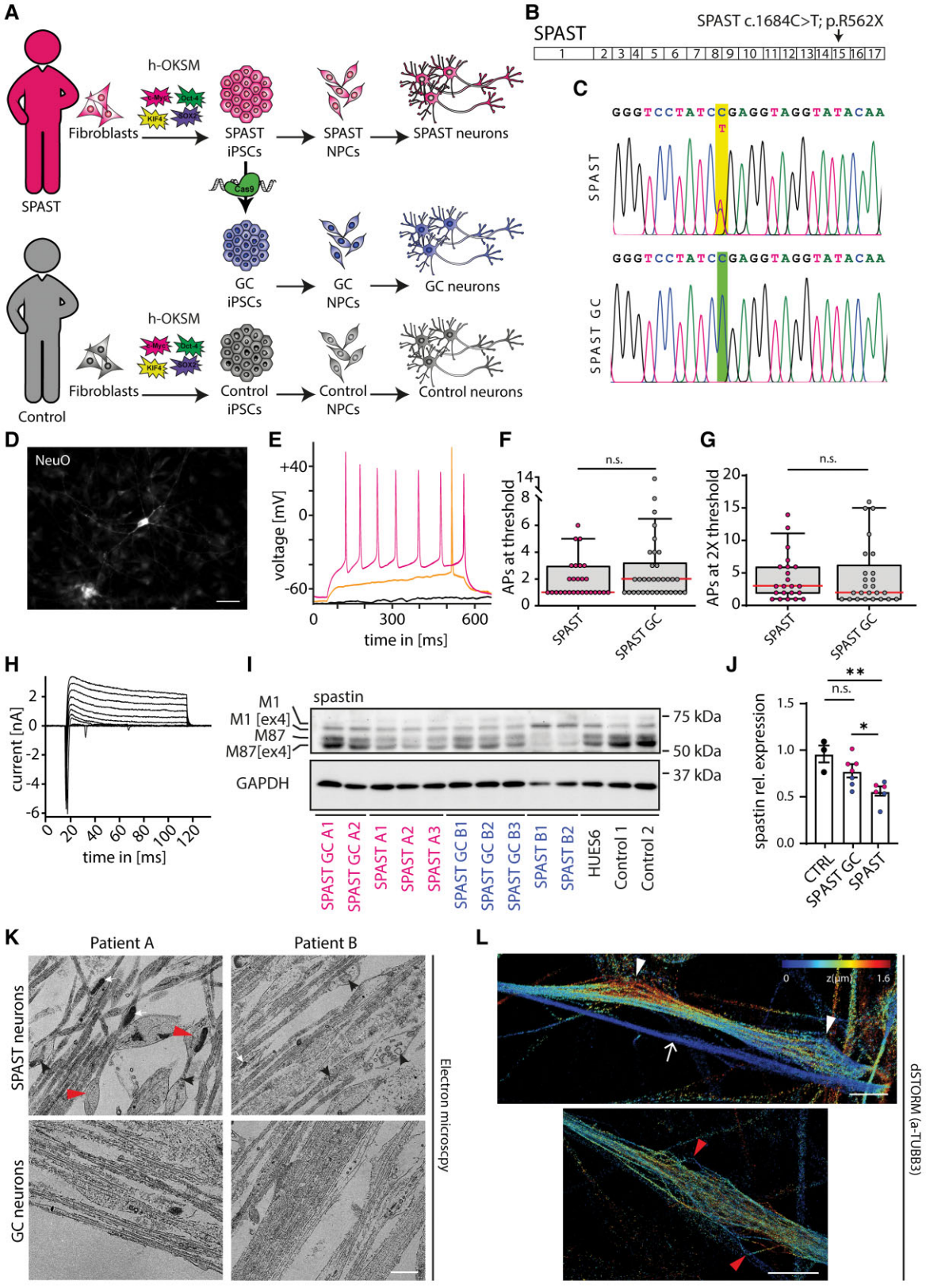

Figure 4 SPAST iPSC-derived neurons to study SOCE are functional and express less spastin. (**A**) Fibroblasts from SPAST patients and healthy donor (Control) were reprogrammed using Yamanaka factors (h-OKSM) to obtain iPSCs. IPSCs are differentiated into neural precursor cells (NPCs) and neurons. One iPSC line per patient was genome-corrected (GC) to generate isogenic controls (GC iPSCs). (**B**) Pathogenic variant in Exon 15 of SPAST patients. (**C**) iPSCs and NPCs were sequenced to confirm genome correction. (**D**) NeuO positive neuron. (**E**) Representative current traces at the holding potential of −70 mV (black trace) at 1-fold (yellow trace) and 2-fold current threshold (magenta trace) in response to depolarizing current injection. (**F**) Number of

(Continued)

start of SOCE, the transport of STIM1 to the PM is slowed down by M1 spastin and DM87 spastin, which, unlike M87, target the ER.

SPAST iPSC-derived neurons to study SOCE are functional and express less spastin

While most spastin *in vitro* studies have been performed by exogenously expressing spastin,[12,13,33] the underlying cause of the human disease SPAST-HSP is most likely a decrease in spastin protein.[11,31,43] Therefore, to study the physiological impact of spastin on the regulation of SOCE on a human neuronal model, we generated iPSC-derived cortical neurons from two previously reported patients (Patients A and B, Fig. 4A, Supplementary Fig. 3 and Supplementary Tables 1 and 2) harbouring an identical heterozygous mutation in *SPAST* Exon 15 c.1684C>T; p.R562X (Fig. 4B and C).[11] We used a previously published embryoid body-based protocol, which generates mainly vGLUT-positive projection neurons with a subpopulation of CTIP2-positive neurons and in addition GFAP-positive astroglia (Supplementary Fig. 3).[11] For this study, additional cortical control neurons came from CRISPR/Cas9 genome-corrected (GC) iPSC lines, which were generated from each of the SPAST patients (isogenic controls, hereafter referred to as SPAST GC A, isogenic line from Patient A or SPAST GC B, isogenic line from Patient B) (Fig. 4A and Supplementary Tables 1 and 2). The *SPAST* gene correction was validated in the genome-corrected iPSCs and NPCs (Fig. 4C) and pluripotency and genetic stability was confirmed in iPSCs by flow cytometry and karyotype analysis and CNV analysis, respectively (data not shown). An iPSC line derived from a healthy individual and one human embryonic stem cell line (HUES6) were added as additional controls (Fig. 4A and Supplementary Tables 1 and 2).

To characterize the electrophysiological function of neurons, we used whole-cell current-clamp to assess the firing behaviour of SPAST compared to SPAST GC and control iPSC-derived neurons (Fig. 4E–G and Supplementary Tables 1–3). We used the neuronal dye NeuroFluor NeuO[44] to localize neurons with similar maturity (Fig. 4D). SPAST derived neurons and SPAST GC neurons generated similar numbers of repetitive action potentials in response to a comparable depolarizing current injection (Fig. 4E–G). In response to depolarizing voltage steps, both, the SPAST neurons and controls displayed sodium and potassium currents (Fig. 4H).

Pathogenic variants in *SPAST* have been shown to result in a decrease in spastin.[11] We thus analysed the expression of spastin in 4-week-old differentiated neurons by western blot. We were able to detect all prototypical spastin isoforms; the neuronal M1-spastin isoform with and without exon four, and the ubiquitously expressed M87-spastin with and without exon four. In addition, SPAST neurons displayed decreased levels of total spastin compared to controls (Fig. 4I and J). In the genome corrected iPSC-derived neurons, the protein levels of spastin were fully recovered to the levels of control neurons (Fig. 4I and J).

One of main hallmarks of SPAST-HSP is the formation of neurite swellings containing disrupted microtubules.[11,32] We therefore conducted electron microscopy to visualize the neurites of SPAST and SPAST GC neurons. Compared to SPAST GC neurons, the axons from SPAST neurons displayed a high number of axonal swellings containing disorganized microtubules, mitochondria, and vesicular structures (Fig. 4K).

To visualize better the microtubule integrity within the swellings formed in SPAST iPSC-derived neurons, we stained the neurons for the neuronal specific β-tubulin subunit, TUBB3, and conducted dSTORM. Using dSTORM, we identified neuronal swellings containing disorganized or disrupted microtubules within the neurites of SPAST-HSP derived neurons (Fig. 4L).

SOCE is impaired in SPAST patient iPSC-derived neurons

Considering the importance of spastin for Ca^{2+} regulation in HEK293T cells, we speculated that neurons derived from patients carrying *SPAST* pathogenic variants would show alterations in Ca^{2+} homeostasis. Since spastin was important for the localization of STIM1 in HEK293 cells, we next analysed the intracellular localization STIM1 in human derived neurons (Fig. 5A). In these cortical neurons, mCherry-STIM1 displayed a reticular and even expression pattern when overexpressed alone. Upon co-expression with M1-spastin, STIM1 redistributed to clusters containing M1-spastin and STIM1 proteins in the soma and along neurites (Fig. 5A), similar to what was observed in HEK cells (Fig. 2). This confirms that M1 spastin is able to alter the distribution of STIM1 in human neurons.

To assess the impact of a decrease in spastin on the neuronal Ca^{2+} homeostasis, we investigated the magnitude of SOCE after Thapsigargin-induced Ca^{2+} store depletion in iPSC-derived neurons (Fig. 5D). The cortical neurons derived from iPSCs carrying a pathological variant in *SPAST*, showed significantly decreased levels of SOCE (Fig. 5D and E). We confirmed by western blot that STIM1 and STIM2 expression was unaltered in iPSC-derived neuronal cultures of SPAST HSP patients compared to controls (Fig. 5B and C). In addition, we did not find any expression changes in GRP78, a marker for ER stress (Fig. 5C), indicating that the impairments in Ca^{2+} regulation by the ER are most likely not induced neither by a change in protein expression nor by a general ER distress in neuronal cultures.

Strikingly, the genome correction of *SPAST* in the isogenic lines, which restored the spastin protein expression (Fig. 4I and J), and axonal swellings (Fig. 4K) was also able to restore Ca^{2+} influx via SOCE to the level of controls (Fig. 5D and E). Importantly, this demonstrates that the precise amount of spastin in neurons is crucial for the regulation of Ca^{2+} via SOCE.

Figure 4 Continued
action potentials generated at 1-fold (Mann–Whitney U = 389, $P = 0.285$. SPAST $n = 27$; *SPAST* GC $n = 34$ cells) and (**G**) 2-fold threshold (Mann–Whitney U = 257, $P = 0.703$; SPAST $n = 22$; *SPAST* GC $n = 25$ cells) were similar between SPAST and *SPAST* GC neurons. Box plot shows the median (red line), the whiskers show the 10th and 90th percentiles. (**H**) Representative potassium and sodium currents in response to depolarizing voltage steps (increment 10 mV). (**I**) Representative western blot of 4-week-old *SPAST*, SPAST GC and Control (HUES6 and control individuals) neurons probed for spastin and GAPDH as housekeeping control. Blot shows the prototypical spastin isoforms expressed in a neuronal culture. M1-spastin with (M1) or without exon four [M1(ex4)] and M87-spastin with (M87) and without exon four [M87(ex4)]. (**J**) Densitometric analysis shows reduction of total spastin protein in SPAST-derived compared to SPAST GC and Control neurons [one-way ANOVA/Holm–Sidak's test $F(2,13) = 8.54$, $P = 0.004$. SPAST versus SPAST GC $P = 0.03$; SPAST versus Control $P = 0.005$; SPAST GC versus Control $P = 0.09$] Each data-point shows the mean spastin expression of 2–5 independent experiments per cell line±*SEM* (controls, black; Patient A, pink; Patient B, blue). (**K**) Electron microscopy of SPAST GC neurons and SPAST neurons showing neurite swellings containing mitochondria (white arrows), disorganized microtubules (red arrows) and vesicles (black arrows). Scale bar = 500 nm. (**L**) dSTORM of swellings (white arrowheads) within SPAST neuron neurites (white arrows) stained with TUBB3. Scale bar = 5 µm. Pseudo-colour bar encodes the z-scale. $^{*}P < 0.05$ $^{**}P < 0.01$ $^{***}P < 0.001$, n.s. = not significant.

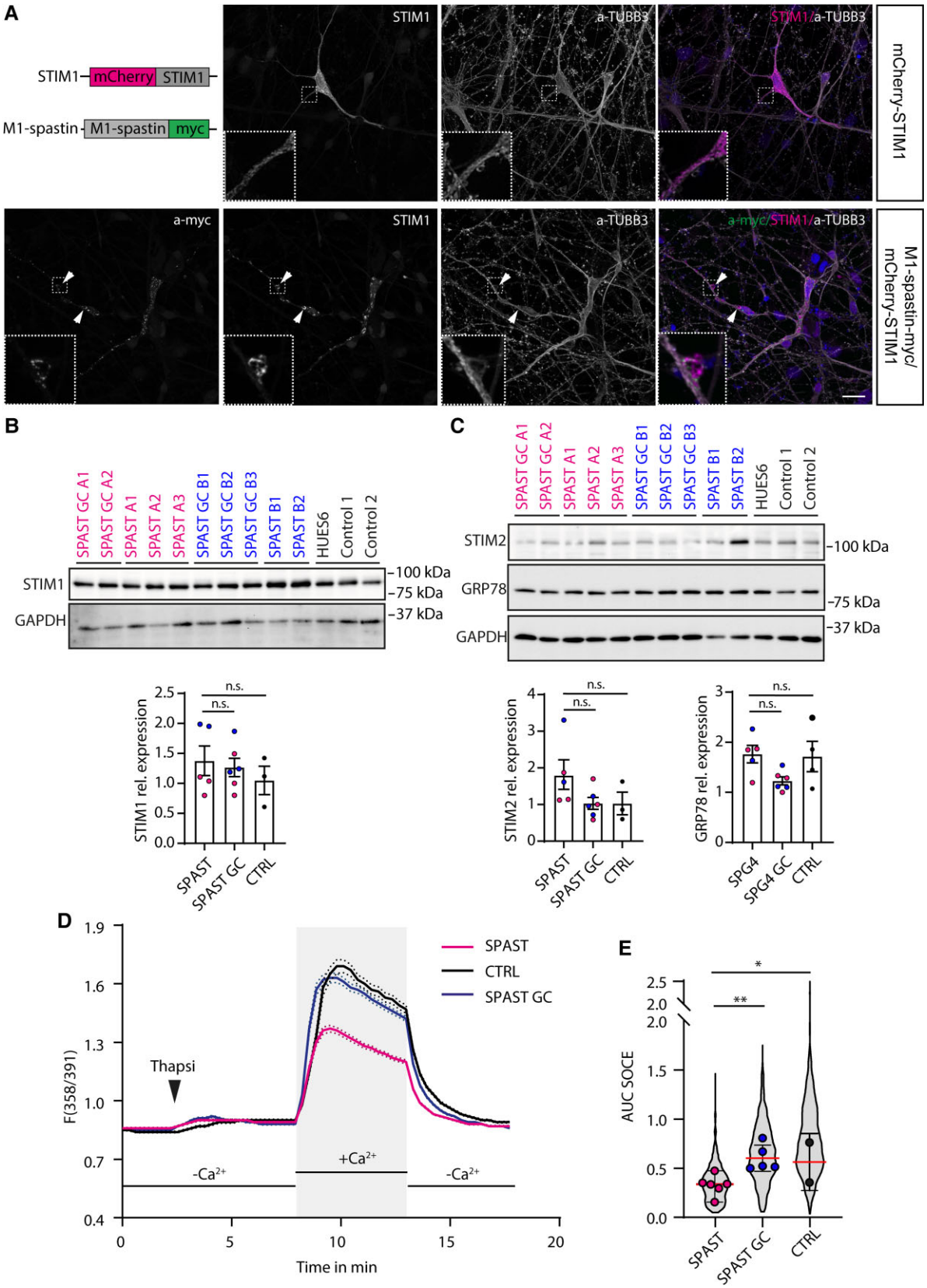

Figure 5 SOCE is impaired in SPAST patient iPSC-derived neurons. (**A**) Four-week-old differentiated control neurons transfected with mCherry-STIM1 display an even distribution of STIM1. In the presence of M1-spastin-myc, mCherry-STIM1 forms clusters containing M1-spastin proteins (white arrowheads). (**B** and **C**) Representative western blot of 4-week differentiated neurons probed for SOCE-linked proteins STIM1 and STIM2 and ER stress marker GRP78. Densitometric analysis showed no difference between SPAST, SPAST GC and healthy groups (CTRL) [one-way ANOVA STIM1 $F(2,11) = 0.49$, $P = 0.63$; STIM2 $F(2,11) = 2.37$, $P = 0.14$; GRP78 $F(2,12) = 2.99$, $P = 0.09$]. Single data-points represent the mean expression per line (2–5 independent

(Continued)

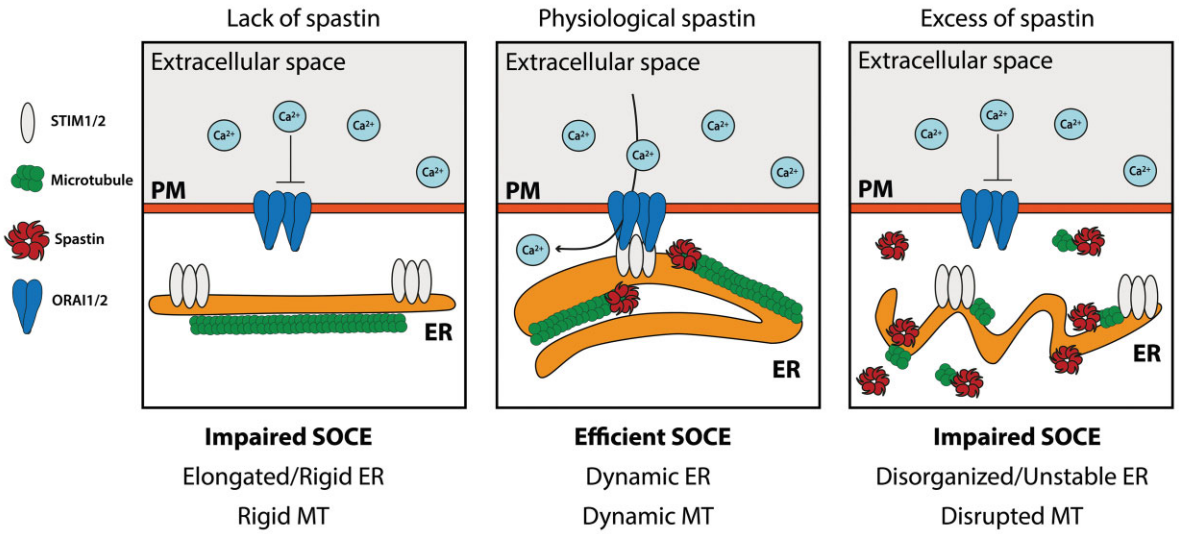

Figure 6 Model for spastin mode of action on the regulation of SOCE. Schematic representation of the proposed effect of spastin on the regulation of SOCE. Lack of spastin decreases the dynamics of the microtubule network necessary to guide the transport of organelles including the ER and ER-resident proteins such as STIM1 to activate SOCE. Excess of spastin shreds the microtubule network decreasing the ER stability, association to the microtubule network, and the directed transport of STIM1 to activate SOCE. Thus, lack or excess of spastin conditions are detrimental for the regulation of SOCE. The model posits that physiological spastin levels are necessary to keep a dynamic ER, microtubule network and uphold an efficient SOCE.

Discussion

Our data show that the reduction of spastin, a microtubule-severing and ER remodelling protein, enlarges the ER and impairs the functional regulation of Ca^{2+} homeostasis. M1 and M87 spastin expression impaired SOCE, which could be reversed by expressing additional STIM1. Spastin is capable of altering STIM1 cluster formation and translocation. Importantly, in human neurons, insufficiency of spastin also altered the regulation of Ca^{2+} homeostasis via SOCE as demonstrated in SPAST patient iPSC derived neurons and isogenic controls. We therefore propose that impaired SOCE contributes to the disease mechanism of SPAST-HSP.

Our results indicate that the presence of spastin is important for SOCE and the maintenance of the ER structure, as lack of spastin in CRISPR/Cas9 KO cells resulted in SOCE reduction and elongated ER. ER structural changes have been previously described in relation to spastin.[45,46] How ER structural changes contribute to the development of HSP is unknown. It is, however, interesting to note that several proteins involved in HSP are directly or indirectly involved in shaping the ER[9,47] and various ER shaping proteins have been linked to the regulation of Ca^{2+} via SOCE, among them Atlastin-1 and Reticulon 4.[16,41,48]

The nature of spastin as a microtubule-severing protein[8] in combination with the observed structural ER alterations, and reduced SOCE in the SPAST KO cells led us to consider a model where spastin acts on the microtubule network, which has an impact on the ER structure, which in turn has an impact on the regulation of Ca^{2+} via SOCE (Fig. 6).

To explore this model, we used overexpression of different spastin isoforms to disassemble the microtubule network and analyse its impact on SOCE and on the transport of STIM1 to the plasma membrane. Resembling the results obtained by others following microtubule depolymerization by nocodazole,[15,49] spastin overexpression reduced SOCE and altered the clustering behaviour of STIM1. Besides depolymerization,[50,51] microtubule hyperstabilization[46,52] has also been reported to interfere with ER structure and SOCE, indicating that both the loss or extreme rigidity of the microtubule network have an impact on the ER structure and SOCE. We postulate that this required balance in microtubule stability for a proper ER function is the reason for observing a similar decrease in SOCE whether we knockout or overexpress spastin (Fig. 6).

While the overexpression of both spastin isoforms reduced SOCE and both induced the intracellular clustering of STIM1 along the ER, only M1 surrounded STIM1 and slowed down the transport of STIM1 to the PM, indicating that M1-spastin is additionally able to retain STIM1 on the ER. Interestingly, a recently discovered shorter neuronal splice variant of STIM1, STIM1B, which lacks the microtubule tracking domain, displays a slower transport towards plasma membrane.[53]

Given its known physiological function, the M87 spastin effects on STIM1 are most likely due to general dysregulation of the microtubule network, while M1-spastin targets more specifically the

Figure 5 Continued
experiments per line). Scatter plot shows the mean of lines±SEM. (**D**) Fura-2 fluorescence ratio changes $F(358/391)$ were analysed in 4-week differentiated iPSC-derived SPAST neurons compared to isogenic SPAST GC neurons and control neurons. Ca^{2+} imaging recording started in absence of Ca^{2+}. For additional depletion of ER Ca^{2+} stores, 2 µM Thapsigargin (Thapsi) was added. Perfusion with Ca^{2+} rich media triggered SOCE, quantified as area under the curve [AUC, grey box. Data shown as mean (line)±95% confidence interval (dotted line)]. (**E**) SOCE is impaired in iPSC-derived neurons from SPAST patients compared to isogenic controls (SPAST GC) and compared to control neurons. SPAST GC isogenic neurons did not differ from control neurons [one-way ANOVA/Holm–Sidak's test $F(2,10) = 9.38$, $P = 0.005$. SPAST ($n = 6$ cell lines) versus SPAST GC ($n = 5$ cell lines) and control ($n = 2$ cell lines). SPAST versus control $P = 0.05$; SPAST versus SPAST GC $P = 0.006$; SPAST GC versus control not significant. $P = 0.69$]. Each data-point represent the median SOCE response of one cell line from 2–5 independent differentiations per cell line. [Scatter plot shows the mean of cell lines (red) ± standard deviation (SD), violin plot shows the distribution of single cells]. (SPAST = 3035 cells; SPAST GC = 3179 cells; Ctrl = 1026 cells) $^{*}P < 0.05$ $^{**}P < 0.01$ $^{***}P < 0.001$, n.s. = not significant.

interaction between the ER and the microtubule network. This interaction might be particularly important for neurons where, unlike other tissues, M1-spastin is abundantly expressed.[11]

Following spastin overexpression the microtubule network is disassembled, allowing us to understand the importance of the microtubule network for the ER shape. However, at endogenous or low spastin expression levels, the microtubule network is conserved and elegantly remodelled by spastin. Therefore, the physiological effect of spastin on the ER and on SOCE may be much more subtle and of a regulatory nature. Moreover, it has been shown that spastin-linked HSP is caused by reduced rather than increased levels of spastin.[11] In addition, different cell types, depending on their morphology and function, have shown disparate SOCE reactions in response to pharmacological alteration of the microtubule network.[16,54]

We thus we switched to a human SPAST patient model to understand whether the alterations in SOCE we observed in the HEK cell model were also detectable in a cell type, which strongly relies on a well-functioning microtubule network.

Our results show that in SPAST patient iPSC-derived neurons, spastin haploinsufficiency is sufficient to impair Ca^{2+} entry after store depletion. The impairment in Ca^{2+} influx is dependent on the expression of spastin, since genome correction via CRISPR/Cas9 was able to restore spastin protein expression, axonal swellings and SOCE efficiency. Altered Ca^{2+} dynamics have been observed across different neurodegenerative diseases giving rise to the 'calcium hypothesis'. This proposes a dysregulation of Ca^{2+} as the underlying basis for a variety of neurodegenerative diseases.[55] Altered SOCE has been described in several studies, including in a genetic iPSC-derived Parkinson's disease model[56] and in a cellular model of the HSP protein atlastin-1.[48] In the latter, both overexpression and atlastin-1 downregulation resulted in altered Ca^{2+} homeostasis.[48]

Very recently and supporting our results, impaired SOCE and elongated ER were detected in a drosophila model for SPAST-HSP, which displayed compromised flight ability.[46] Similar flight deficiencies have been reported in flies with impaired SOCE caused by *dStim1* and *dOrai1* pan-neuronal downregulation, demonstrating the importance of SOCE for the fly movement.[57] Together, these findings emphasize the importance of effective SOCE for motor neuron function.

The SPAST iPSC-derived neurons displayed axonal swellings with accumulated mitochondria and disorganized microtubules, which has been described as an important *in vitro* hallmark of SPAST-HSP studies.[11,32] The onset of SPAST-HSP is rather slow, suggesting that while pathogenic variants in *SPAST* affect cellular mechanisms early on, chronic exposure to additional stressors may trigger the disease onset. Different stressors including ageing processes have been linked to a reduction in the ability of cells to regulate SOCE.[58] Thus, dysfunction in spastin combined with additional stressors affecting Ca^{2+} regulation (e.g. ageing) could promote the disease onset. This hypothesis should be further tested *in vitro* and *in vivo*.

In conclusion, our data define a new role of spastin at the interface between ER and microtubule dynamics. Changes in the expression of spastin disturb the regulation of neuronal Ca^{2+} homeostasis, and thus impact the susceptibility and vulnerability of cortical axons in SPAST-HSP.

Acknowledgements

We thank Evan Reid, Steven Havlicek, Angelika Lampert and Iryna Prots for fruitful discussions. We thank Evan Reid, Rachel Allison and Guy Pearson for sharing the spastin constructs used to generate the IRES-GFP vectors. We thank Holger Wend, Michaela Farrell, Sonja Plötz and Eva Kunzelmann for excellent technical assistance, Philipp Tripal and Benjamin Schmidt from the Optical Imaging Center Erlangen for help with microscopy and Cataldo Schietroma from Abbelight for his assistance with dSTORM data. We thank Ute Hehr for her help in sequencing, and Mandy Krumbiegl and André Reis for help with karyotyping of iPSCs. We thank Deborah Bennett for her help with English language editing. Parts of this work were performed in partial fulfillment of the requirements for obtaining the title Dr.rer.nat of Tania Rizo. This work is dedicated to our patients and controls.

Funding

This project was funded by the Förderverein für HSP-Forschung and the Deutsche Forschungsgemeinschaft (DFG, German Research Foundation)—WI 3567/2-1). B.W. and T.R. are members of the research training group 2162 'Neurodevelopment and Vulnerability of the Central Nervous System' of the Deutsche Forschungsgemeinschaft (DFG, German Research Foundation—270949263/GRK2162). Additional support came from the IZKF advanced projects E30 (B.W., J.W.) E27 (M.F.) and IZKF Junior Project J66 and rotation fellowship to E.E. Further support came from the Research Foundation Medicine at the University Clinic Erlangen, Germany the Bavarian Ministry of Science and the Arts in the framework of the ForInter network, from the German Federal Ministry of Education and Research TreatHSP consortium (BMBF 01GM1905B and 01EK1609B) and from the Tom Wahlig Foundation. B.N. was supported by the Deutsche Forschungsgemeinschaft (CRC1027-C4; CRC894-A2 and TRR219-C09). P.A. was supported by the Deutsche Forschungsgemeinschaft (CRC877-A13, grant number 125440785).

Competing interests

The authors report no competing interests.

Supplementary material

Supplementary material is available at *Brain* online.

References

1. Hazan J, Fonknechten N, Mavel D, *et al*. Spastin, a new AAA protein, is altered in the most frequent form of autosomal dominant spastic paraplegia. Article. *Nat Genet*. 1999;23(3):296–303.
2. Depienne C, Tallaksen C, Lephay JY, *et al*. Spastin mutations are frequent in sporadic spastic paraparesis and their spectrum is different from that observed in familial cases. *J Med Genet*. 2006;43(3):259–265.
3. Schule R, Wiethoff S, Martus P, *et al*. Hereditary spastic paraplegia: Clinicogenetic lessons from 608 patients. *Ann Neurol*. 2016;79(4):646–658.
4. Schwarz GA, Liu CN. Hereditary (familial) spastic paraplegia; further clinical and pathologic observations. *AMA Arch Neurol Psychiatry*. 1956;75(2):144–162.
5. Deluca GC, Ebers GC, Esiri MM. The extent of axonal loss in the long tracts in hereditary spastic paraplegia. *Neuropathol Appl Neurobiol*. 2004;30(6):576–584.
6. Claudiani P, Riano E, Errico A, Andolfi G, Rugarli EI. Spastin subcellular localization is regulated through usage of different translation start sites and active export from the nucleus. *Exp Cell Res*. 2005;309(2):358–369.

7. Roll-Mecak A, Vale RD. Structural basis of microtubule severing by the hereditary spastic paraplegia protein spastin. *Nature*. 2008;451(7176):363–367.
8. Vemu A, Szczesna E, Zehr EA, *et al*. Severing enzymes amplify microtubule arrays through lattice GTP-tubulin incorporation. *Science*. 2018;361(6404):eaau1504.
9. Rao K, Stone MC, Weiner AT, *et al*. Spastin, atlastin, and ER relocalization are involved in axon but not dendrite regeneration. *Mol Biol Cell*. 2016;27(21):3245–3256.
10. Mancuso G, Rugarli EI. A cryptic promoter in the first exon of the SPG4 gene directs the synthesis of the 60-kDa spastin isoform. *BMC Biol*. 2008;6:31.
11. Havlicek S, Kohl Z, Mishra HK, *et al*. Gene dosage-dependent rescue of HSP neurite defects in SPG4 patients' neurons. *Hum Mol Genet*. 2014;23(10):2527–2541.
12. Papadopoulos C, Orso G, Mancuso G, *et al*. Spastin binds to lipid droplets and affects lipid metabolism. *Plos Genet*. 2015;11(4): e1005149.
13. Plaud C, Joshi V, Kajevu N, Pous C, Curmi PA, Burgo A. Functional differences of short and long isoforms of spastin harboring missense mutation. *Dis Model Mech*. 2018;11(9):dmm033704.
14. Stutzmann GE, Mattson MP. Endoplasmic reticulum Ca(2+) handling in excitable cells in health and disease. *Pharmacol Rev*. 2011;63(3):700–727.
15. Smyth JT, DeHaven WI, Bird GS, Putney JW Jr. Role of the microtubule cytoskeleton in the function of the store-operated Ca2 + channel activator STIM1. *J Cell Sci*. 2007;120(Pt 21):3762–3771.
16. Chang CL, Chen YJ, Quintanilla CG, Hsieh TS, Liou J. EB1 binding restricts STIM1 translocation to ER-PM junctions and regulates store-operated Ca(2+) entry. *J Cell Biol*. 2018;217(6):2047–2058.
17. Grigoriev I, Gouveia SM, van der Vaart B, *et al*. STIM1 is a MT-plus-end-tracking protein involved in remodeling of the ER. *Curr Biol*. 2008;18(3):177–182.
18. Putney JW J. A model for receptor-regulated calcium entry. *Cell Calcium*. 1986;7(1):1–12.
19. Hirve N, Rajanikanth V, Hogan PG, Gudlur A. Coiled-coil formation conveys a STIM1 signal from ER lumen to cytoplasm. *Cell Rep*. 2018;22(1):72–83.
20. Samtleben S, Wachter B, Blum R. Store-operated calcium entry compensates fast ER calcium loss in resting hippocampal neurons. *Cell Calcium*. 2015;58(2):147–159.
21. Lalonde J, Saia G, Gill G. Store-operated calcium entry promotes the degradation of the transcription factor Sp4 in resting neurons. *Sci Signal*. 2014;7:328.
22. Segal M, Korkotian E. Roles of calcium stores and store-operated channels in plasticity of dendritic spines. *Neuroscientist*. 2016; 22(5):477–485.
23. Secondo A, Bagetta G, Amantea D. On the role of store-operated calcium entry in acute and chronic neurodegenerative diseases. *Front Mol Neurosci*. 2018;11:87.
24. Dhanya SK, Hasan G. Purkinje neurons with loss of STIM1 exhibit age-dependent changes in gene expression and synaptic components. *J Neurosci*. 2021;41(17):3777–3798.
25. Wu J, Ryskamp DA, Liang X, *et al*. Enhanced store-operated calcium entry leads to striatal synaptic loss in a Huntington's Disease mouse model. *J Neurosci*. 2016;36(1):125–141.
26. Kawamata H, Ng SK, Diaz N, *et al*. Abnormal intracellular calcium signaling and SNARE-dependent exocytosis contributes to SOD1G93A astrocyte-mediated toxicity in amyotrophic lateral sclerosis. *J Neurosci*. 2014;34(6):2331–2348.
27. Nikonov AV, Hauri HP, Lauring B, Kreibich G. Climp-63-mediated binding of microtubules to the ER affects the lateral mobility of translocon complexes. *J Cell Sci*. 2007;120(Pt 13):2248–2258.
28. Terasaki M, Chen LB, Fujiwara K. Microtubules and the endoplasmic reticulum are highly interdependent structures. *J Cell Biol*. 1986;103:1557–1568.
29. Levente J, Keitaro T, Andrew K, *et al*. Reticulon 4 is necessary for endoplasmic reticulum tubulation, STIM1-Orai1 coupling, and store-operated calcium entry. *J Biol Chem*. 2014;289:9380–9395.
30. Mannan AU, Boehm J, Sauter SM, *et al*. Spastin, the most commonly mutated protein in hereditary spastic paraplegia interacts with Reticulon 1 an endoplasmic reticulum protein. journal article. *Neurogenetics*. 2006;7(2):93–103.
31. Denton KR, Lei L, Grenier J, Rodionov V, Blackstone C, Li XJ. Loss of spastin function results in disease-specific axonal defects in human pluripotent stem cell-based models of hereditary spastic paraplegia. *Stem Cells*. 2014;32(2):414–423.
32. Rehbach K, Kesavan J, Hauser S, *et al*. Multiparametric rapid screening of neuronal process pathology for drug target identification in HSP patient-specific neurons. *Sci Rep*. 2019;9(1):9615.
33. Allison R, Edgar JR, Pearson G, *et al*. Defects in ER-endosome contacts impact lysosome function in hereditary spastic paraplegia. *J Cell Biol*. 2017;216(5):1337–1355.
34. Takahashi K, Tanabe K, Ohnuki M, *et al*. Induction of pluripotent stem cells from adult human fibroblasts by defined factors. *Cell*. 2007;131(5):861–872.
35. Haeussler M, Schonig K, Eckert H, *et al*. Evaluation of off-target and on-target scoring algorithms and integration into the guide RNA selection tool CRISPOR. *Genome Biol*. 2016;17(1):148.
36. Brinkman EK, Chen T, Amendola M, van Steensel B. Easy quantitative assessment of genome editing by sequence trace decomposition. *Nucleic Acids Res*. 2014;42(22):e168.
37. Allison R, Lumb JH, Fassier C, *et al*. An ESCRT-spastin interaction promotes fission of recycling tubules from the endosome. *J Cell Biol*. 2013;202(3):527–543.
38. Alansary D, Schmidt B, Dorr K, *et al*. Thiol dependent intramolecular locking of Orai1 channels. *Sci Rep*. 2016;6:33347.
39. Dittert I, Vlachova V, Knotkova H, *et al*. A technique for fast application of heated solutions of different composition to cultured neurones. *J Neurosci Methods*. 1998;82(2):195–201.
40. Asano N, Hampel U, Garreis F, *et al*. Differentiation patterns of immortalized human meibomian gland epithelial cells in three-dimensional culture. *Invest Ophthalmol Vis sci*. 2018;59(3): 1343–1353.
41. Jozsef L, Tashiro K, Kuo A, *et al*. Reticulon 4 is necessary for endoplasmic reticulum tubulation, STIM1-Orai1 coupling, and store-operated calcium entry. *J Biol Chem*. 2014;289(13):9380–9395.
42. Pascual-Caro C, Berrocal M, Lopez-Guerrero AM, *et al*. STIM1 deficiency is linked to Alzheimer's disease and triggers cell death in SH-SY5Y cells by upregulation of L-type voltage-operated Ca(2+) entry. *J Mol Med (Berl)*. 2018;96(10):1061–1079.
43. Riano E, Martignoni M, Mancuso G, *et al*. Pleiotropic effects of spastin on neurite growth depending on expression levels. *J Neurochem*. 2009;108(5):1277–1288.
44. Er JC, Leong C, Teoh CL, *et al*. NeuO: a fluorescent chemical probe for live neuron labeling. *Angew Chem Int Ed Engl*. 2015;54(8):2442–2446.
45. Park SH, Zhu PP, Parker RL, Blackstone C. Hereditary spastic paraplegia proteins REEP1, spastin, and atlastin-1 coordinate microtubule interactions with the tubular ER network. *J Clin Invest*. 2010;120(4):1097–1110.
46. Vajente N, Norante R, Redolfi N, Daga A, Pizzo P, Pendin D. Microtubules stabilization by mutant spastin affects er morphology and Ca(2+) handling. *Front Physiol*. 2019;10:1544.
47. Giudice T L, Lombardi F, Santorelli FM, Kawarai T, Orlacchio A. Hereditary spastic paraplegia: clinical-genetic characteristics and evolving molecular mechanisms. *Exp Neurol*. 2014;261: 518–539.

48. Li J, Yan B, Si H, Peng X, Zhang SL, Hu J. Atlastin regulates store-operated calcium entry for nerve growth factor-induced neurite outgrowth. *Sci Rep*. 2017;7:43490.
49. Oka T, Hori M, Ozaki H. Microtubule disruption suppresses allergic response through the inhibition of calcium influx in the mast cell degranulation pathway. *J Immunol*. 2005;174(8):4584–4589.
50. Terasaki M, Chen LB, Fujiwara K. Microtubules and the endoplasmic reticulum are highly interdependent structures. *J Cell Biol*. 1986;103(4):1557–1568.
51. Joensuu M, Belevich I, Rämö O, *et al*. ER sheet persistence is coupled to myosin 1c-regulated dynamic actin filament arrays. *Mol Biol Cell*. 2014;25(7):1111–1126.
52. Joensuu M, Jokitalo E. ER sheet–tubule balance is regulated by an array of actin filaments and microtubules. *Exp Cell Res*. 2015;337(2):170–178.
53. Ramesh G, Jarzembowski L, Schwarz Y, *et al*. A short isoform of STIM1 confers frequency-dependent synaptic enhancement. *Cell Rep*. 2021;34(11):108844.
54. Galan C, Dionisio N, Smani T, Salido GM, Rosado JA. The cytoskeleton plays a modulatory role in the association between STIM1 and the Ca2 + channel subunits Orai1 and TRPC1. *Biochem pharmacol*. 2011;82(4):400–410.
55. Schrank S, Barrington N, Stutzmann GE. Calcium-handling defects and neurodegenerative disease. *Cold Spring Harb Perspect Biol*. 2020;12(7):a035212.
56. Korecka JA, Talbot S, Osborn TM, *et al*. Neurite collapse and altered ER Ca(2+) control in human Parkinson disease patient iPSC-derived neurons with LRRK2 G2019S mutation. *Stem Cell Rep*. 2019;12(1):29–41.
57. Venkiteswaran G, Hasan G. Intracellular Ca2 + signaling and store-operated Ca2 + entry are required in Drosophila neurons for flight. *Proc Natl Acad Sci U S A*. 2009;106(25):10326–10331.
58. Calvo-Rodriguez M, Garcia-Durillo M, Villalobos C, Nunez L. In vitro aging promotes endoplasmic reticulum (ER)-mitochondria Ca(2+) cross talk and loss of store-operated Ca(2+) entry (SOCE) in rat hippocampal neurons. *Biochim Biophys Acta*. 2016;1863(11):2637–2649.